



Microphysical Transience of Warm Season Precipitation in the Southern Appalachians:

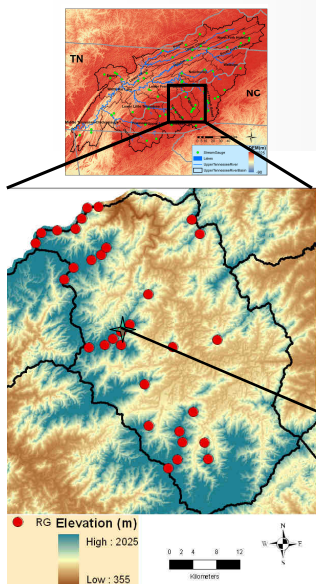
Toward Physical Retrieval

Anna Wilson, Yajuan Duan and Ana P. Barros

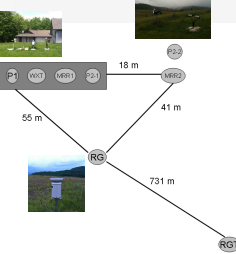
Department of Civil and Environmental Engineering, Pratt School of Engineering, Duke University, NC



1. Introduction - Study Area



The maps to the left show the locations of the high elevation tipping bucket rain gauge (RG) network that has been collecting data in this study region since 2007. Intensive observing periods using Micro-Rain Radars and other instrumentation have been conducted yearly since installation of the network, primarily during the warm season. The star is shown to mark the location of a concentrated cross-calibration period conducted during May-June 2012. During this period, the radars were collocated with Hydrological Services tipping bucket rain gauges at 0.1 mm resolution, Vaisala automated weather stations and Parsivel optical disdrometers. Images of the instrumentation are shown below.



2. TRMM PR 2A25, V6 vs. V7

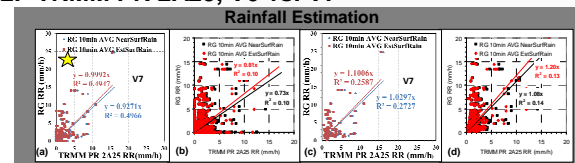


Figure 1 - Scatterplots for the comparison TRMM 2A25 surface rain rate and averaged rain gauge rain rates for the period 06/2008-05/2012. For all rain gauge records and TRMM 2A25 surface rain rates in V7(a) and V6(c); For non-null rain gauge records and TRMM 2A25 surface rain rates in V7(b) and V6(d). Rain gauge rain rates are averaged using a 10-min scale centered at the time the satellite overpasses. (b) and (d) are from Pratt and Barros (2010).

Table 1 - TRMM 2A25 V7(V6)/RG performance comparison as a function of the time scale (10-, 20-, 30-min). Definition of performance parameters is reported below. The statistics for V7 are during 06/2008 - 05/2012, for V6 (in parentheses) are during 06/2008 - 05/2009.

	Time window (min)									Perfect Score
	10min			20min			30min			
	All	0XX	1XX	All	0XX	1XX	All	0XX	1XX	
Accuracy ¹	0.97(0.95)	0.96(0.95)	0.97(0.95)	0.96(0.94)	0.97(0.95)	0.96(0.94)	0.96(0.94)	0.96(0.94)	0.96(0.94)	1
FB ²	1.98(0.59)	5.16(0.66)	1.02(0.54)	1.36(0.51)	2.99(0.58)	0.76(0.47)	1.07(0.46)	2.36(0.52)	0.63(0.42)	1
POD ³	0.31(0.30)	0.09(0.36)	0.61(0.35)	0.42(0.33)	0.17(0.33)	0.72(0.33)	0.48(0.31)	0.20(0.32)	0.77(0.31)	1
FAR ⁴	0.38(0.4)	0.53(0.46)	0.37(0.35)	0.43(0.36)	0.56(0.44)	0.45(0.3)	0.49(0.34)	0.52(0.39)	0.52(0.3)	0
POFD ⁵	0.01(0.01)	0.01(0.02)	0.01(0.01)	0.01(0.01)	0.01(0.02)	0.02(0.01)	0.02(0.01)	0.01(0.01)	0.03(0.01)	0
TS ⁶	0.26(0.29)	0.08(0.27)	0.45(0.3)	0.32(0.28)	0.14(0.26)	0.46(0.29)	0.33(0.27)	0.17(0.27)	0.42(0.27)	1

¹Accuracy = $YY + NNJ / Total$; ²Frequency Bias = $FB = YY + YN / (YY + NY)$; ³Probability of detection = $POD = YY / (YY + NY)$; ⁴False alarm rate = $FAR = NY / (YY + NY)$; ⁵Probability of False Detection = $POFD = NY / (NN + NY)$; ⁶Threat Score = $TS = YY / (YY + NY + YN)$. RG0XX: catchment size of 200mm; 0.2mm/min) and TB30.1 (RG1XX: catchment size of 282.8mm; 0.1mm/min).

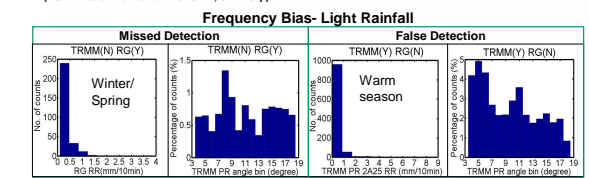


Figure 2 - Histograms for the TRMM 2A25 V7 overpass characteristics: Missed detection and False detection. Percentage is calculated over the total counts in each angle bin. (06/2008 - 05/2012).

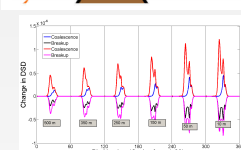
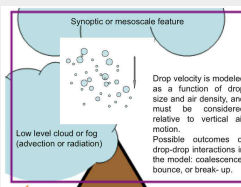
3. Model Description

The explicit raindrop population dynamics model simulates the microphysical processes occurring in the rainshaft between the cloud base and the ground surface, which may include not only interactions between raindrops but also raindrops with cloud water from lower level cloud or fog. A simplified representation of the idealized column model is shown at right. Observations from the vertically pointing radar are used to provide boundary conditions for the model, which solves the stochastic collection-breakup equation, in order to simulate the evolution of microphysical properties (drop size distribution, rain intensity and hydrometeor type) through time and space and gain insight into the processes (autoconversion, overcoiling synoptic conditions, terrain contributions) that drive this evolution. The initial drop size distributions are tracked through an entirely physical evolution downward through the column and forward in time.

The governing equation for the model is presented below. The terms highlighted in red represent the contribution to the number concentration in each drop size bin from coalescence and breakup respectively. The terms highlighted in green represent the loss due to those processes.

$$\frac{dN_i(t)}{dt} = \sum_{j=1}^{i-1} \sum_{k=i-j}^i \underbrace{N_j N_k}_{\text{Coalescence}} - \sum_{k=i+1}^{\infty} \underbrace{N_i N_{k-i}}_{\text{Breakup}} - \underbrace{N_i}_{\text{Removal}}$$

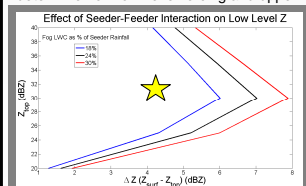
The contribution of coalescing drops to the n^{th} bin, calculated to preserve number and mass: $x_i \leq v \leq x_{i+1} \Rightarrow \eta = \frac{x_{i+1} - v}{x_{i+1} - x_i}$, $x_{i+1} \leq v \leq x_i \Rightarrow \eta = \frac{v - x_{i+1}}{x_i - x_{i+1}}$



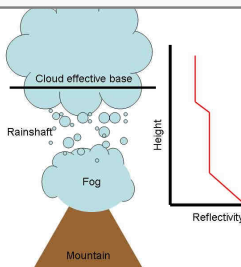
4. Methodology

Top Boundary Condition: Two methods are used to find the top boundary condition. **Method 1:** When there is a clearly defined bright band, the maximum reflectivity (Z) above 1 km is found. Then, the level observing at least 10% less than that value (in dBZ) is chosen as the top boundary condition. This threshold for bright band follows Zhang et al 2008. **Method 2:** When there is not a clearly defined bright band, the top boundary condition is chosen based on the Z gradient throughout the column, as in the simplified schematic below right.

Low Level Forcing: This area has a persistent fog regime; without including this forcing it is impossible to achieve the observed vertical structure and rain intensity and accumulation at the ground. A sensitivity study was conducted to determine how low level forcing and upper level Z interact. The plot at left

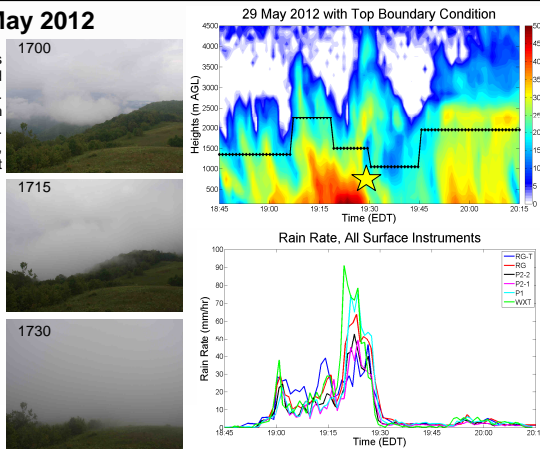


shows Z differences across the column after equilibrium has been achieved in each simulation. The 24% curve was used to introduce a fog DSD into the simulation, with drop diameters ranging from 10-160 microns. Mature fog with larger drop sizes was used here since fog had been observed on the ground by webcam for over one hour prior to the onset of rain.



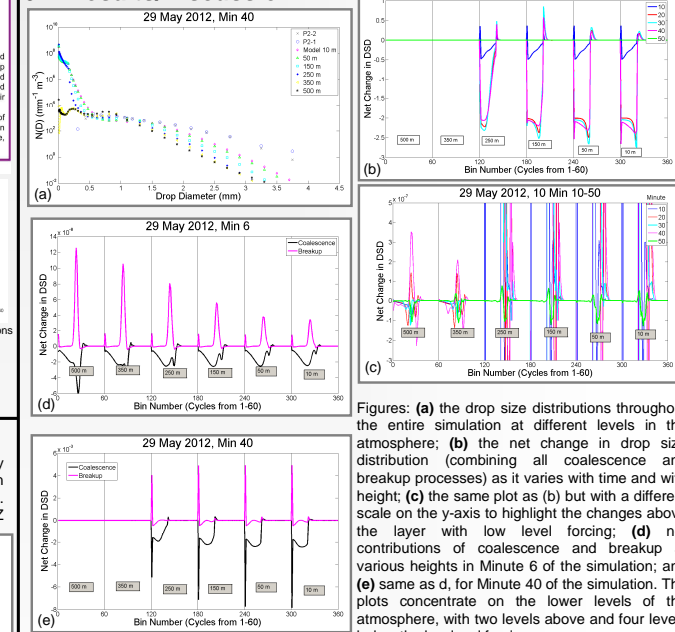
5. Case Study - 29 May 2012

In the case study described in this panel, there is not a clearly defined bright band through most of the event. This case is an early evening, warm season shallow convective event. Method 2 is used until 1951 local time, and Method 1 is then used for the rest of the simulation.

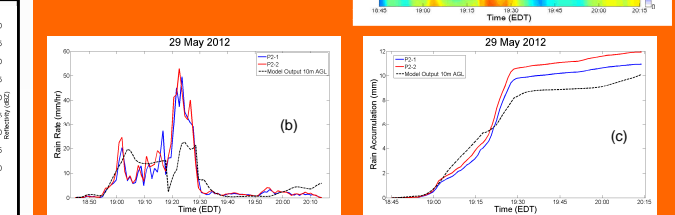


Images above left were taken by a webcam at the location approximately one hour before the simulation starts. Plots at far left show the evolution throughout the day of temperature and relative humidity. A plot of the rain rate observed at the surface during the event is shown above.

6. Results/Discussion



Figures: (a) the drop size distributions throughout the entire simulation at different levels in the atmosphere; (b) the net change in drop size distribution (combining all coalescence and breakup processes) as it varies with time and with height; (c) the same plot as (b) but with a different scale on the y-axis to highlight the changes above the layer with low level forcing; (d) net contributions of coalescence and breakup at various heights in Minute 6 of the simulation; and (e) same as d, for Minute 40 of the simulation. The plots concentrate on the lower levels of the atmosphere, with two levels above and four levels below the low level forcing.



Critical Research Needs - Results corroborate the localized importance of persistent fog interacting with cloud to intensify or trigger precipitation events that are often experienced only at high elevations and contribute significantly to the yearly water budget of the region. Even though seeder-feeder interactions between orographic rainfall systems and low level clouds and fog can cause reflectivity increases up to 20% in the lower 1 km of the atmosphere, the literature lacks any DSD observations of these systems that can be used for microphysical modeling and to incorporate physically-based corrections into retrieval algorithms.

7. Acknowledgements/References

This research was supported by the NASA PMM program and is based upon work supported by the National Science Foundation on NSF Grant No. 1106401.
 Prat, O.P. and A.P. Barros, 2010: Assessing satellite-based precipitation estimates in the Southern Appalachian mountains using rain gauges and TRMM PR. *Adv. Geosci.*, 25, 143-153.
 Prat, O.P. and A.P. Barros, 2007: A robust numerical solution of the stochastic collection-breakup equation for warm rain. *J. Appl. Meteor. Climatol.*, 46, 1480-1497.
 Zhang, J., C. Langston and K. Howard, 2008: Brightband identification based on vertical profiles of reflectivity from the WSR-88D. *J. Atmos. Oceanic Technol.*, 25, 1859-1872.
 Our work could not be done without the support of students, private and public landowners, and colleges in western North Carolina. We thank especially the National Park Service; Paul Super, Greg Wilson and Pamela McCown; Asheville-Buncombe Technical Community College and UNC Asheville; and REI student Daniel Morf.